Desorption characteristics of H_2O and CO_2 from alumina F200 under different feed/purge pressure ratios and regeneration temperatures

Yun Fei Shi[a], Xiang Jun Liu[a]*, Yu Guo[a], Mohammad Ali Kalbassi[b], Ying Shu Liu[a]

[a]School of Energy and Environmental Engineering, University of Science & Technology Beijing, Beijing 100083，China

[b]Brunel University of London, Uxbridge, UB8 3PH, United Kingdom

* Corresponding author.   E-mail:liuxj@me.ustb.edu.cn   Tel:+86 10 62333792

Abstract

Air pre-purification is an important process for industrial air separation with cryogenic distillation method. This process is typically realized by pressure swing adsorption or temperature swing adsorption. H_2O and CO_2 are the two major components to be removed among the contaminants. In this paper, we establish a mathematical model describing the mass and heat balances in the adsorption bed, and the double-component adsorption/desorption equilibriums of H_2O/CO_2 on alumina F200. To conduct desorption performance analysis, a one-cycle process consisting of feed, blowdown, and purge step under different operating conditions, such as feed/purge pressure ratio and regeneration temperature, is numerically studied. The effect of heat on the desorption performance of H_2O and CO_2 is investigated by changing the purge gas temperature within 30 °C to 200 °C under feed/purge pressure ratios of 6:1.1 and 10:1.1, respectively. Detailed results of the H_2O and CO_2 adsorption/desorption behaviors in the bed are demonstrated. The mass and heat transfer characteristics during desorption are also analyzed. Suggestions on the optimization of the heating temperature and duration of purge gas are also proposed.

Keywords: Air purification; Alumina F200; H_2O and CO_2 desorption; Heat and mass transfer

1 Introduction

Air pre-purification is a required process in industrial production of oxygen and nitrogen with the distillation method. Such contaminants as H_2O and CO_2 should be removed before air is cryogenically cooled to a liquid state, because these impurities are solidified during the cooling process and may thus block the vessels (Kerry 2007). Adsorption separation technology is being widely used for this purpose, and two methods are generally used in terms of adsorbent regeneration: Temperature Swing Adsorption (TSA) and Pressure Swing Adsorption (PSA). Adsorbents in TSA are totally regenerated by heating, but only partially regenerated by counter-current purge gas in PSA. PSA requires no additional energy for heating, but has high switch losses due to its short cycle time, and vice versa in TSA (Kerry 2007, Yang 1987). Both methods have their own advantages and disadvantages.

Many studies have been carried out to improve the conventional PSA and TSA methods and reduce the total energy consumption needed for air pre-purification. Oliker (1982) proposed a method of operating adsorption beds that are regenerable with heat by altering the timing of the beginning and termination of the adsorption, regeneration and cooling stage to reduce energy consumption. Thermally Enhanced PSA (TEPSA) was proposed based on conventional PSA cycle by using a heated purge gas of around 70 °C (Kalbassi et al. 1997). The aim of TEPSA is to extend the cycle time of PSA so as to lower switch losses. Kumar et al. (2002) suggested a multi-bed PSA pre-purification unit by removing water and carbon dioxide in separate beds. The unit uses constant and continual pressurization throughout the cycle and does not vent purified feed gas to the atmosphere. Thermal pressure swing adsorption (TPSA) (Wright et al. 2005) uses hot gas of around 100 °C to regenerate the downstream part (CO_2 adsorption zone), whereas part of the upstream area (H_2O adsorption zone) was also regenerated by the heat. This can significantly reduce the required heating energy compared with

a full TSA cycle according to the study. Schmidt et al. (2008) proposed a hybrid PSA/TSA system that can adjust the quantity of heat to be provided by the regeneration gas as a function of temperature data, which were taken within a strategic portion of the water selective adsorbent zone. Hidano et al. (2011) reduced the cost of adsorption vessel by 30% by using a high flow-rate method in a TSA air purification system. Zhang and Wang (2013) proposed a three-bed TSA system, which can achieve energy savings of 29.5% by recovering and reusing the effluent purge gas. However, most of those improvements are empirical discoveries based on experiments. Further theoretical understanding of the H_2O and CO_2 adsorption/desorption behaviors, especially the desorption behavior, is required to guide the design of a more efficient system for air pre-purification.

In this paper, a comprehensive mathematical model of H_2O/CO_2 double-component adsorption and desorption in a fixed bed packed with alumina F200 is established. Based on pore volume filling theory, the H_2O/CO_2 double-component adsorption and desorption equilibriums are described by combining two single-component isotherm equations, the F–G equation for H_2O, and the Freundlich equation for CO_2. A one-cycle process consisting of feed, blowdown, and purge is numerically studied under feed/purge pressure ratios of 6:1.1 and 10:1.1 respectively. The effect of heat on the desorption performance of H_2O and CO_2 is also studied by changing the purge gas temperature within 30 °C to 200 °C under each feed/purge pressure ratio. Detailed results of H_2O and CO_2 adsorption/desorption behaviors in the bed are demonstrated. The mass and heat transfer characteristics during desorption are also analyzed. Suggestions on the optimization of the heating temperature and duration time of purge gas are proposed.

2 Mathematical models of H_2O/CO_2 adsorption and desorption in fixed bed

A mathematical model is developed to numerically study the two-component adsorption and

desorption of H_2O/CO_2 in a fixed bed of alumina F200. The bed is used to remove water vapor and carbon dioxide from air. The model is based on the following assumptions: (a) the gas and solid phase are assumed to have constant physical properties and that the gas phase follows the ideal gas law; (b) the pressure drop along the bed is negligible; (c) the adsorption of N_2 and O_2 are negligible, (d) heat transfer resistance between the gas and solid phase is neglected, (e) the bed is well insulated and can be regarded as adiabatic, and (f) the problem is one-dimensional and only axial changes are considered.

This study aims to reveal the desorption characteristics of H_2O and CO_2 on alumina F200 under different feed pressures and regeneration temperatures. Thus, only one cycle consisting of feed, blowdown, and purge step is simulated. Pressure change during the cycle is illustrated in Fig. 1. The durations of $0 \sim t_1$, $t_1 \sim t_2$, and $t_2 \sim t_3$ represent the feed, blowdown, and purge steps, respectively. The pressure change during blowdown step is characterized by

$$p = p_{end} - (p_{start} - p_{end})(1 - t/t_s)^2,$$ (1)

where t_s is the duration time of the pressure changing step.

2.1 Mass and Energy Conservation Equations

The mass balance equation for component i is expressed as

$$\frac{\partial y_i}{\partial t} + u \frac{\partial y_i}{\partial x} - D_{ax} \frac{\partial^2 y_i}{\partial x^2} + \frac{\rho_b RT}{\varepsilon p} \left(\frac{\partial \overline{q}_i}{\partial t} - y_i \sum_j \frac{\partial \overline{q}_j}{\partial t} \right) = 0,$$ (2)

where y is the molar fraction, $\overline{q}$ is the mean adsorbed amount in adsorbent pellets, [mol/kg], u is the interstitial velocity, [m/s], ε is the bed porosity, ρ_b is the bulk density of adsorbent in the bed, [kg/m^3], and D_{ax} is the axial dispersion coefficient. The axial dispersion coefficient can be estimated by using (Edwards and Richardson 1968)

$$D_{ax} = \gamma_1 D_m + \frac{u d_p / 2}{1 + 13 \gamma_1 D_m / u d_p},$$ (3)

where $\gamma_1 = 0.45 + 0.55\varepsilon$. The interstitial velocity can be determined from the overall mass balance equation expressed as

$$T\frac{\partial(u/T)}{\partial x} = \frac{1}{T}\frac{\partial T}{\partial t} - \frac{1}{p}\frac{dp}{dt} - \frac{\rho_b RT}{\varepsilon p}\sum_j \frac{\partial \overline{q}_j}{\partial t}, \tag{4}$$

The energy balance equation is expressed as

$$\left(\rho_g c_{p,g} + \frac{\rho_b}{\varepsilon}c_{p,s}\right)\frac{\partial T}{\partial t} + \rho_g c_{p,g}u\frac{\partial T}{\partial x} - \lambda_{ax}\frac{\partial^2 T}{\partial x^2} = \frac{\rho_b}{\varepsilon}\sum_j \left(\left|\Delta H_j\right| + c_{p,g}M_g T\right)\frac{\partial \overline{q}_j}{\partial t} + \frac{dp}{dt}, \tag{5}$$

where $c_{p,g}$ and $c_{p,s}$ are the specific heat of the gas and solid phases, respectively; [J·kg^{-1}·K^{-1}], ΔH is the isosteric heat of adsorption; and [J/mol], λ_{ax} is the axial thermal conductivity. The adsorption rate $\partial \overline{q}/\partial t$ can be determined by the Linear Driving Force (LDF) model given by

$$\frac{\partial \overline{q}_i}{\partial t} = k_i\left(q_i^* - \overline{q}_i\right), \tag{6}$$

where q^* is the equilibrium adsorbed amount, and k is the mass transfer coefficient. The mass transfer coefficient can be estimated by using

$$k = \frac{15\varepsilon_p}{r_p^2}\left(\frac{c}{\rho_s q^*}D_p + D_s\right), \tag{7}$$

where ε_p is the porosity of pellet, r_p is the radius of pellet, ρ_s is the density of pellet, c is the concentration at the surface of pellet, and q^* is the adsorbed amount equilibrium with c, D_p is the gas phase diffusivity through pores and D_s is the adsorbed phase diffusivity through walls of pores. D_p can be estimated from

$$\frac{1}{D_p} = \tau\left(\frac{1}{D_m} + \frac{1}{D_k}\right) \tag{8}$$

where τ is the tortuosity of pellet, and D_m can be estimated through (Bird et al. 2002)

$$\frac{pD_{AB}}{(p_{c,A}p_{c,B})^{1/3}(T_{c,A}T_{c,B})^{5/12}(1/M_A + 1/M_B)^{1/2}} = a\left(\frac{T}{\sqrt{T_{c,A}T_{c,B}}}\right)^b \tag{9}$$

where T_c, P_c are the critical temperature and pressure, M is the molecular mass, T is the temperature,

[K], and p is the total pressure [atm]. The unit of D_{AB} is [cm²/s]. For CO_2-N_2 pair, $a=2.745e-4$,

$b=1.823$; for H_2O-N_2 pair, $a=3.640e-4$, $b=2.334$. D_k can be estimated by (Kauzmann 1966)

$$D_k = 9.7 \times 10^3 r_{pore} \left(\frac{T}{M} \right)^{1/2} \qquad (10)$$

where r_{pore} is the mean radius of pores, [cm], T is the temperature, [K], and M is the molecular mass.

The unit of D_k is [cm²/s]. Surface diffusion is more significant when the concentration is very high, so

the D_s of H_2O cannot be neglected in this work. According to Desai et al. (1992), the D_s of H_2O on

alumina is estimated as $3.0e-10$ m²/s from experimental data. The D_s of CO_2 is neglected in this work.

2.2 Adsorption and desorption equilibriums of H_2O/CO_2 mixture on alumina F200

The pore volume filling theory (Doong and Yang 1988) provides a practical way to describe the

equilibrium behavior of arbitrary two-component adsorption. By combining the Freundlich–Gaussian

(F–G) equation (Liu et al. 2013) for H_2O and the Freundlich equation for CO_2, a two-component

adsorption isotherm model for H_2O/CO_2 competitive adsorption on F200 proposed by Liu et al. (2014)

is obtained. The models are respectively expressed as

$$\begin{aligned} q_1^* &= \frac{q_{s1} A_1 (1 - A_2)}{1 - A_1 A_2} \\ q_2^* &= \frac{q_{s2} A_2 (1 - A_1)}{1 - A_1 A_2} \end{aligned} \qquad (11)$$

where

$$\begin{aligned} A_1 &= A_{1,a} + A_{1,b} \\ A_2 &= (p_2 / p_{s2})^{k_2 T} \\ A_{1,a} &= q_{s1,a} / q_{s1} (p_1 / p_{s1})^{k_{1,a} T} \\ A_{1,b} &= q_{s1,b} / q_{s1} \text{erf} \left[k_{1,b} T^{-1} / \ln (p_{s1} / p_1) \right] \\ q_{s1} &= q_{s1,a} + q_{s1,b} \end{aligned} \qquad (12)$$

In the equations above, $q_{s1,a}$ is the maximal adsorbed amount of H_2O in micropores and on macropore

walls, $q_{s1,b}$ is the maximal adsorbed amount of H_2O in macropores due to capillary condensation, q_{s2}

is the saturated adsorbed amount of CO_2, and p_{s1} and p_{s2} are the saturated vapor pressure of H_2O and CO_2.

The fitting results of the adsorption and desorption equilibrium isotherms of H_2O on F200 are shown in Fig. 2, and the corresponding parameters are listed in Table 1. The fitting results of CO_2 adsorption data (Li et al. 2009) on F200 are shown in Fig. 3, and the corresponding parameters are listed in Table 2. The experimental desorption data of H_2O are obtained by taking out the irreversible part of the original data provided by Serbezov (2003). In this way, once the partial pressure is reduced to zero, the equilibrium adsorbed amount during adsorption/desorption cycle becomes zero.

The adsorption/desorption isotherm of H_2O usually exhibits hysteresis caused by capillary condensation/evaporation. Determining adsorption/desorption branches can be done in several ways according to the adsorption/desorption history (Hefti and Mazzotti, 2014). In this work, different branches of the desorption isotherm are obtained by shrinking the capillary-condensation/evaporation-based part, as demonstrated below. The desorption isotherm that starts from the saturation point is expressed as

$$q_{de} = q_{m,de} x^{k_{m,de}T} + q_{c,de},$$ (13)

where $q_{c,de}$ represents the part due to capillary condensation/evaporation, which is expressed as

$$q_{c,de} = a_1 \exp[-b_1(x-c_1)^2] + a_2 \exp[-b_2(x-c_2)^2].$$ (14)

The desorption isotherm branch that starts from $x=x_i$ can be expressed as

$$q_{de} = q_{m,de} x^{k_{m,de}T} + \left(q_{ad}(x_i) - q_{m,de} x_i^{k_{m,de}T}\right) \frac{q_{c,de}(x)}{q_{c,de}(x_i)}.$$ (15)

Fig. 4 demonstrates how the desorption branch for a specific location in the bed is determined according to its adsorption/desorption history. Take state point A for instance, the state undergoes desorption since $q_A > q_{ad}(x_A)$. The uptake at the equilibrium is determined by the desorption branch

that starts from point B as long as the local relative humidity keeps dropping. If the local relative humidity increases, say the current local equilibrium state is at point C, then the equilibrium uptake remains unchanged until the local relative humidity goes higher than that of point D. Following this process, the equilibrium uptake can be determined from the adsorption branch. If the local state is within the region below the adsorption branch, the equilibrium uptake should be directly determined from the adsorption branch.

2.3 Boundary conditions

The adsorption/desorption cycle consists of feed, blowdown, and purge step. The boundary conditions for each step are listed in Table 3.

2.4 Numerical methods

The abovementioned governing equations are discretized with the finite volume method, individually solved with the tri-diagonal matrix algorithm (TDMA) method, and then coupled by iteration. The first-order upwind scheme and the second-order central difference scheme are used to approximate the first- and second-order spatial derivatives, respectively.

3 Results and discussion

3.1 Description of the adsorption bed and its operating conditions

The adsorption bed has a height of 2 m and a diameter of 0.2 m. The adsorbent pellet has a diameter of 1.8 mm. Other properties of the bed, adsorbent, and adsorbates used in the model are listed in Table 4. The feed flow rate is 120 Nm^3/h, and the flow rate ratio of purge to feed is set as 0.45, that is, the purge flow rate is 54 Nm^3/h. The purge gas is pure nitrogen. The relative humidity of the feed air is 100%, and the volume fraction of CO_2 in the feed air is 370 ppm. Other operating conditions are given in Table 5.

3.2 Desorption characteristics under different feed/purge pressure ratios

Two different feed pressures, 6 bar and 10 bar, are set for comparative study and noted as case a and case b, respectively. The purge gas temperature is 30 °C, and the purge pressure is set as 1.1 bar in both cases. The duration of feed step is determined by avoiding the breakthrough of CO_2 (CO_2 breakthroughs earlier than H_2O on alumina), which means that feed step is finished when the concentration of CO_2 at the outlet is 0.01 ppm. In this way, the determined durations of feed step are 59.0 min in case a and 96.4 min in case b. The duration of the blowdown step is set as 2 min in both cases. The durations of purge step are 57.0 min for case a and 94.4 min for case b. The detailed operating parameters of case a and b are given in Table 6.

Simulated results of cases a and b are presented together for comparison in Figs. 5 to 8. The distributions of concentration along the bed height for the H_2O and CO_2 components at the end of adsorption are shown in Fig. 5. As can be seen, high feed pressure enlarges the distance between the adsorption frontiers of H_2O and CO_2. Note that the relative humidity of the feed air is 100%, indicating that the partial pressure of H_2O is its saturated vapor pressure at the feed temperature, which does not change in both cases. In other words, the volume fraction of H_2O in the feed air drops from 6972 ppm to 4180 ppm as the feed pressure increases from 6 bar to 10 bar. For CO_2, the volume fraction in the feed air remains unchanged, but the partial pressure increases from 222 Pa to 370 Pa. The adsorption capability of the adsorbent for CO_2 increases slower with pressure due to its isotherm nonlinearity. This means the adsorption frontier of CO_2 moves faster as its partial pressure increases. Thus, the distance between the adsorption frontiers of CO_2 and H_2O is larger in case b.

Fig. 6 shows the variation of the total adsorbed amount with cycle time for H_2O and CO_2. The total adsorbed amount of H_2O at the end of adsorption is barely changed in both cases, whereas that of CO_2

is significantly increased in case b. The amount of H_2O fed into the bed can be calculated by using

$$m_{H_2O} = \frac{p_s}{p_0} \times \frac{M_{H_2O}}{M_{air}} \times \dot{m} \times \Delta t , \tag{16}$$

where p_s is the saturated vapor pressure of H_2O, p_0 is the total bed pressure, M represents molar mass, $\dot{m}$ is the mass flow rate of the feed air, and Δt is the duration time of feed step. Here, p_s only depends on the feed temperature, which along with $\dot{m}$ and molar masses, remains unchanged in both cases. Thus,

$$\frac{m_{H_2O, \text{ case a}}}{m_{H_2O, \text{ case b}}} = \frac{p_{\text{case b}}}{p_{\text{case a}}} \times \frac{\Delta t_{\text{case a}}}{\Delta t_{\text{case b}}} = \frac{10}{6} \times \frac{59.0}{96.4} = 1.02 , \tag{17}$$

which explains the observation that the total amount of adsorbed H_2O is barely changed in both cases.

Fig. 7 shows the distribution of temperature as well as the uptakes of H_2O and CO_2 along the bed height at the ends of the feed step and purge step. The location of the temperature profile's rising edge is in accordance with the adsorption frontier of H_2O, because most of the heat is mainly produced by water adsorption. The lower temperature rise during adsorption in case b is due to the increase of gas phase's volumetric heat capacity, which is proportional to the bed pressure. The distributions of uptake for CO_2 and H_2O along the bed height are in accordance with their concentration profiles shown in Fig. 5. The water adsorption zone is limited to a very short portion of the bed (less than 10%), while the CO_2 adsorption zone occupies the major portion, which ranges from 80% to 90%.

The variation of the total adsorbed amount with time for CO_2 and H_2O during desorption is shown in Fig. 8. As illustrated in Tables 7 and 8, the ratio of the total amount of desorbed to adsorbed H_2O varies from 73.55% to 86.47%, whereas that for CO_2 varies from 64.27% to 74.27% as the feed/purge pressure ratio changes from 6:1.1 to 10:1.1. Hence, we can conclude that the desorption performance, which is represented by the ratio of the total desorbed amount during blowdown and purge step to the total adsorbed amount during feed step, increases as the feed/purge pressure ratio increases.

Moreover, the desorption performance of CO_2 is poorer than that of H_2O in the pressure swing adsorption cycle. The ratio of the total amount of desorbed to adsorbed H_2O is 73.55% in case a, whereas that for CO_2 is only 64.27%. This may be due to the differences in the types of their adsorption/desorption isotherms. Fig. 9 shows the dimensionless isotherms of H_2O and CO_2. Here, p_0 represents the partial pressure of each component in the feed air, and q_0 represents the corresponding single-component equilibrium uptake. According to Brunauer's classification of adsorption isotherms, the isotherm of CO_2 is of type I, whereas the isotherm of H_2O is of type IV. As demonstrated in Fig. 9, the dimensionless equilibrium uptake of CO_2 drops more slowly than that of H_2O with the same decrement of dimensionless pressure. Consequently, a small partial pressure change for H_2O could lead to a larger desorbed amount than that of CO_2. Therefore, the desorption performance of pressure swing on CO_2 is inferior to that on H_2O. Hence, system improvements should focus on enhancing the desorption of CO_2.

3.3 Desorption characteristics under different regeneration temperatures

The effect of heat on H_2O/CO_2 desorption is studied in this section by heating the purge gas to four different levels. The temperatures of the purge gas at each level are 30 °C, 60 °C, 120 °C, and 200 °C, respectively.

3.3.1 Effect of heat on H_2O/CO_2 desorption in case a

Fig. 10 shows the distributions of temperatures and uptakes of the H_2O and CO_2 components along the bed height at dimensionless desorption times of 1/6, 1/3, 2/3, and 1/1 in case a. The variation of the total adsorbed amount of each component with time during desorption is shown in Fig. 11. The velocity of the purge gas can be determined by

$$u = \frac{Q_{v,std}}{\varepsilon A} \frac{p_{std}}{p_{purge}} \frac{T_{purge}}{T_{std}}, \tag{18}$$

which is proportional to the regeneration temperature. However, the speed levels of the movements of the temperature frontier at different levels of regeneration temperature, as seen in Fig. 10, are almost the same. This can be explained that movement speed of the heat frontier depends primarily on the heat capacity ratio of gas phase to solid phase. As illustrated in Fig. 12(a), the temperature profile along the bed height for gas and solid phases during purge step normally features a heat transfer zone as well as the temperature difference between the two phases. The profile can be idealized as a sharp frontier, as illustrated in Fig. 12(b). Without considering the isosteric heat of adsorption, energy balance analysis on the elemental volume yields

$$u\rho_g c_{p,g}(T_p - T_0)\varepsilon A dt = (\rho_b c_{p,s} + \varepsilon\rho_g c_{p,g})(T_p - T_0)A dx,\tag{19}$$

where $dx/dt = \tilde{u}$ is defined as the movement speed of the heat frontier, A is the cross-sectional area of the bed, and T_p is temperature of the purge gas. The term on the left-hand side represents the net heat introduced into the volume, whereas the term on the right-hand-side represents the increase of the volume's total internal energy. The balance of the two terms determines how fast the heat could move compared with the velocity of gas flow. Thus, we have

$$\frac{\tilde{u}}{u} = \frac{\varepsilon\rho_g c_{p,g}}{\varepsilon\rho_g c_{p,g} + \rho_b c_{p,s}} \approx \frac{\varepsilon\rho_g c_{p,g}}{\rho_b c_{p,s}},\tag{20}$$

which indicates that the movement speed of the heat frontier is usually much smaller than the velocity of the purge gas as $\varepsilon\rho_g c_{p,g} \ll \rho_b c_{p,s}$. Substituting Eq. (15) into Eq. (17), and with the ideal gas law applied, the movement speed of the heat frontier is obtained:

$$\tilde{u} = \frac{\varepsilon u\rho_g c_{p,g}}{\rho_b c_{p,s}} = \varepsilon \frac{Q_{v,std}}{\varepsilon A}\frac{p_{std}}{p_{purge}}\frac{T_{purge}}{T_{std}}\frac{p_{purge}}{R_g T_{purge}}\frac{c_{p,g}}{\rho_b c_{p,s}} = \frac{Q_{v,std}}{A}\frac{p_{std}}{R_g T_{std}}\frac{c_{p,g}}{\rho_b c_{p,s}} = \frac{Q_{v,std}}{A}\frac{\rho_{g,std}c_{p,g}}{\rho_b c_{p,s}}$$

$$= \frac{54}{3600\times\pi\times 0.2^2/4}\times\frac{1.293\times 1005}{870\times 784}\,[\text{m/s}] = 0.0009\,[\text{m/s}]\tag{21}$$

which is independent of the temperature and pressure of the purge gas. The subscript *std* stands for

the standard condition, which is 1 atm and 0 ℃. The dimensionless value with respect to bed height of 2 m and desorption time of 59.0 min is given by

$$\tilde{u} = 0.0009[\text{m/s}] \times \frac{59.0\ [\text{min}]}{2.0\ [\text{m}]} \times 60[\text{s/min}] = 1.59 . \tag{22}$$

As seen from Fig. 11, no distinctive effect on different grades of heat can be seen on the desorptions of H_2O and CO_2 before the dimensionless desorption times of 0.60 and 0.35, respectively. This is because the heat frontier does not reach their main adsorption zones to enhance desorption. At the dimensionless desorption time of 0.35, when the heat frontier reaches a dimensionless height of around 0.5, the heat takes effect on the desorption of CO_2, as illustrated in Figs. 10(b) and 11(b). At the dimensionless desorption time of 0.60, when the heat frontier reaches the bottom end of the bed in which the adsorbed H_2O is concentrated, the heat takes effect on the desorption of H_2O, as illustrated in Figs. 10(c) and 11(a). Note that there exists a significant temperature drop at the bottom end due to a large amount of H_2O being desorbed. The desorption of CO_2 is in accordance with the movement of the heat. The uptake of CO_2 within the area where the heat reaches is significantly reduced, as shown in Figs. 10(b)–(d).

Table 7 presents a detailed analysis of the desorption performance under different regeneration temperatures. The ratios of the total amount of desorbed to adsorbed CO_2 are increased to 84.49% and 99.99% as the regeneration temperatures are lifted to 60 °C and 120 °C, respectively. The desorption performance of CO_2 is remarkably improved and is very close to that of H_2O through the additional regeneration heat. However, the improvement is not always in proportion to the increase of regeneration temperature. As seen from Fig. 11(b), the variation of the total adsorbed amount with desorption time for CO_2 under regeneration temperature of 200 °C barely differs from the result under regeneration temperature of 120 °C. This may be due to the fact that the change rate of

equilibrium uptake with temperature drops down much slower as temperature increases (shown in Fig. 13b). The drop rate is 0.001 $mol \cdot kg^{-1} \cdot ℃^{-1}$ between the regeneration temperature of 30 ℃ and 60 ℃. The rate becomes less than 6% between 120 ℃ and 200 ℃. This finding indicates that extra heat is of little use for enhancing desorption when the regeneration temperature exceeds a certain level. The appropriate purge gas temperature in this case would be ranging from 60 ℃ to 120 ℃, but closer to 120 ℃.

The additional heat in the purge gas is mainly used for improving the desorption performance of CO_2. Although the desorption of CO_2 is accelerated by injecting high-grade heat, a little portion of the heat is absorbed during the desorption process. There is no need to sustain the bed temperature on a high level once CO_2 is completely desorbed. The duration of the heated purge gas can be determined by the desorption rate under the corresponding regeneration temperature, which is reflected as a mass transfer zone, as shown in Figs. 10(b) and 10(c). A low regeneration temperature leads to low desorption rate and, therefore, a wide mass transfer zone. The width of the mass transfer zone for CO_2 under a regeneration temperature of 120 ℃ has the dimensionless height of about 0.2~0.3. Thus, the duration of the heat should be the width divided by the dimensionless movement speed of the heat frontier, that is, 0.13~0.19 of the dimensionless desorption time.

3.3.2 Effects of heat on H_2O/CO_2 desorption in case b

The distributions of temperature and uptakes of the H_2O and CO_2 components along the bed height at the dimensionless desorption times of 1/6, 1/3, 2/3, and 1/1 in case b are shown in Fig. 14. The variation of total adsorbed amount of each component with time during desorption is shown in Fig. 15. As seen from the figure, the no-heat-effect stage for H_2O is about 0~0.35 of the dimensionless desorption time and about 0~0.15 of the dimensionless desorption time for CO_2. This can be

explained by the movement of heat, whose dimensionless speed with respect to bed height of 2 m and desorption time of 96.4 min is given by

$$\tilde{u} = 0.0009 \text{ [m/s]} \times \frac{96.4 \text{ [min]}}{2.0 \text{ [m]}} \times 60 \text{ [s/min]} = 2.60 \,, \tag{23}$$

At dimensionless desorption time of 0.15 when the heat takes effect on the desorption of CO_2 as illustrated in Fig. 14(a) and Fig. 15(b), the heat frontier reaches dimensionless height of around 0.6. At dimensionless desorption time of 0.35 when the heat takes effect on the desorption of H_2O as illustrated in Fig. 14(b) and Fig. 15(a), the heat frontier reaches dimensionless height of around 0.1.

Table 8 presents a detailed analysis of the desorption performances under different regeneration temperatures. As analyzed in case a, there exists an appropriate level of regeneration heat, which is sufficient for improving the desorption performance of CO_2. Given that the difference between the results under the regeneration temperature of 120 ℃ and 200 ℃ is quite small, as shown in Fig. 15(b), and that the desorption performance of CO_2 can be improved up to 94.56% as the regeneration temperature is lifted to 60 ℃, then the appropriate regeneration temperature for this case would be between 60 ℃ and 120 ℃, specifically closer to 60 ℃. It has been shown in Fig. 6 that high feed/purge pressure ratio results in high performance of desorption. Thus, the lower grade of heat in this case is sufficient for desorption enhancement.

As mentioned previously, sustaining the temperature of purge gas at a high level for the duration of the purge step is unnecessary. The duration of the heat pulse can be estimated from the width of the mass transfer zone, as shown in Figs. 14(a) and 14(b). The width of the main mass transfer zone is about the dimensionless height of 0.2~0.3. Thus, the duration should be the width divided by the dimensionless movement speed of the heat frontier, that is, 0.08~0.12 of the dimensionless desorption time.

4 Conclusions

The desorption characteristics of H_2O and CO_2 on alumina F200 under different feed/purge pressure ratios and regeneration temperatures are numerically studied through one-cycle process simulation. High feed/purge pressure ratio can improve the desorption performance while enlarge the distance between the adsorption frontiers of H_2O and CO_2. The desorption performance of CO_2 is poorer compared with that of H_2O without additional regeneration heat. The high level of regeneration heat can improve the desorption performance of CO_2 more significantly than H_2O by counter-current purge flow. However, this has an optimal value. A higher level of heat is needed as the feed/purge pressure ratio decreases; these should be around 120 ℃ and 60 ℃ for feed/purge pressure ratios of 6:1.1 and 10:1.1, respectively. The duration of the additional heat can also be reduced as most of the heat is only used to heat up the bed, whereas few of them are absorbed by the desorption process. A heat pulse of 0.13~0.19 of the desorption time is appreciated for feed/purge pressure ratio of 6:1.1, while a heat pulse of 0.08~0.12 of the desorption time is appreciated for feed/purge pressure ratio of 10:1.1.

Reference

Bird R.B., Stewart, W.E., Lightfoot, E.N.: Transport Phenomena. John Wiley & Sons, Inc., New York, 2002.

Desai R., Hussain M., Ruthven D.M., Adsorption on activated alumina. II – kinetic behavior. The Canadian Journal of Chemical Engineering 70(4), 707-715 (1992).

Doong, S.J.; Yang, R.T.: A simple potential-theory model for predicting mixed-gas adsorption, Ind. Eng. Chem. Res. 27(4), 630-635 (1988).

Edwards, M.F., Richardson, J.F.: Gas dispersion in packed beds. Chem. Eng. Sci. 23(2), 109-123 (1968).

Hefti, M., Mazzotti, M.: Modeling water vapor adsorption/desorption cycles. Adsorption 20(2) 359-371 (2014).

Hidano, T., Nakamura, M., Nakamura, A., Kawai, M.: The downsizing of a TSA system for an air purification unit using a high flow rate method. Adsorption 17(4), 759-763 (2011).

Kalbassi, M.A., Golden, T.C.: Purification of gases using solid adsorbents. US Patent 5614000 A, 1997.

Kauzmann W.: Kinetic Theory of Gases. Benjamin, New York, 1966.

Kerry, F.G.: Industrial Gas Handbook: Gas Separation and Purification. CRC Press, New York, 2007.

Kumar, R., Mcllroy, C., Schluter, R., Pulsinelle. J., Mitariten, M.: Multi-bed adsorption process for air purification. US Patent 20020139246 A1, 2002.

Li, G., Xiao, P., Webley, P.: Binary adsorption equilibrium of carbon dioxide and water vapor on activated alumina, Langmuir 25(18), 10666-10675 (2009).

Liu, X.J., Shi, Y.F., Kalbassi, M.A., Underwood, R., Liu, Y.S.: Water vapor adsorption isotherm expressions based on capillary condensation, Sep. Purif. Technol. 116, 95-100 (2013).

Liu, X.J., Shi, Y.F., Kalbassi, M.A., Underwood, R., Liu, Y.S.: A comprehensive description of water vapor equilibriums on alumina F-200: adsorption, desorption, and H_2O/CO_2 binary adsorption. Sep.

Purif. Technol. 133(8), 276–281 (2014).

Oliker, M.D.: Adsorption beds and method of operation thereof. US Patent 4324564 A, 1982.

Rege, S.U., Yang, R.T., Qian, K., Buzanowski, M.A.: Air prepurification by pressure swing adsorption using single/layered beds. Chem. Eng. Sci. 56(8), 2745-2759 (2001).

Ribeiro, A.M., Sauer, T.P., Grande, C.A., Moreira, R.F.P.M., Loureiro, J.M., Rodrigues, A.E.: Adsorption equilibrium and kinetics of water vapor on different adsorbents, Ind. Eng. Chem. Res. 47(18), 7019-7026 (2008).

Schmidt, W.P., Zwilling, D.P., Wright, A.D., Kalbassi, M.A., Raiswell, C.J.: Control scheme for hybrid PSA/TSA systems. US Patent 7413595 B2, 2008.

Wright, A.D., Kalbassi, M.A., Golden, T.C.: Prepurification of air using an advanced thermal-pressure swing adsorption (Tpsa) cycle. AIChE Annual Meeting, New York, 2005.

Yang, R.T.: Gas Separation by Adsorption Process. Butterworth Publishers, Boston, 1987.

Yagi, S.; Kunii, D., Endo, K.: Heat transfer in packed beds through which water is flowing. Int. J. Heat Mass Transfer 7(3), 333-339 (1964).

Zhang, P., Wang, L.: Comparative study on the performance of adsorbent bed regenerated by clean and used purge gas heating. Ind. Eng. Chem. Res. 52(45), 15912-15922 (2013).

Table captions

Table 1 Parameters of the H_2O adsorption/desorption isotherm model on alumina F200

Table 2 Parameters of the CO_2 adsorption isotherm model on alumina F200

Table 3 Boundary conditions for feed, blowdown and purge step

Table 4 Properties used in the mathematic model

Table 5 Operating Conditions

Table 6 Duration time of each step

Table 7 Desorption performance analysis for case a

Table 8 Desorption performance analysis for case b

Figure captions

Fig. 1 Pressure change with time in the studied cycle ($0 \sim t_1$ is feed step, $t_1 \sim t_2$ is blowdown step, $t_2 \sim t_3$ is purge step).

Fig. 2 Fitting of the H_2O adsorption/desorption equilibrium data on alumina F200 (the multiple lines are results of fitting at temperature of 5, 15, 25, 35 ℃).

Fig. 3 Fitting of the CO_2 adsorption isotherm data on alumina F200.

Fig. 4 Different branches of the H_2O desorption isotherm at 30 ℃.

Fig. 5 Distribution of concentration along the bed height for H_2O and CO_2 at the end of feed step in both cases investigated in present study.

Fig. 6 Variation of total uptake with time for H_2O and CO_2 during one cycle in both cases investigated in present study.

Fig. 7 Distribution of temperature and uptakes of H_2O and CO_2 along the bed height at the ends of feed step and purge step in both cases investigated in present study.

Fig. 8 Variation of dimensionless total adsorbed amount in the bed with dimensionless desorption time for H_2O and CO_2 in both cases investigated in present study.

Fig. 9 Dimensionless adsorption/desorption isotherm for H_2O and CO_2 at 30 ℃.

Fig. 10 Distribution of temperature and uptakes of H_2O and CO_2 along the bed height at 1/6, 1/3, 2/3 and 1/1 of desorption time in case a (solid lines, 30 ℃; dashed lines, 60 ℃; dotted lines, 120 ℃; dash-dotted lines, 200 ℃).

Fig. 11 Variation of dimensionless total adsorbed amount in the bed for H_2O and CO_2 with dimensionless desorption time under different purge gas temperature in case a.

Fig. 12 Energy balance analysis on an elementary volume of the bed during purge step (**Fig. a**: normal

temperature profile along the bed height; **Fig. b**: idealized temperature profile along the bed height neglecting heat transfer resistance and axial thermal dispersion).

Fig. 13 Variation of equilibrium uptake with temperature for H_2O and CO_2 under different partial pressure.

Fig. 14 Distribution of temperature and uptakes of H_2O and CO_2 along the bed height at 1/6, 1/3, 2/3 and 1/1 of desorption time in case b (solid lines, 30 ℃; dashed lines, 60 ℃; dotted lines, 120 ℃; dash-dotted lines, 200 ℃).

Fig. 15 Variation of dimensionless total adsorbed amount in the bed for H_2O and CO_2 with dimensionless desorption time under different purge gas temperature in case b.

Table 1 Parameters of the H$_2$O adsorption/desorption isotherm model on alumina F200

	$q_{s1,a}^{*}$	$q_{s1,b}^{*}$	$k_{1,a}^{\dagger}$	$k_{1,b}^{\ddagger}$				
adsorption	5.483	16.87	1.600E-3	39.11				
	$q_{m,de}^{*}$	$k_{m,de}^{\dagger}$	a_1	b_1	c_1	a_2	b_2	c_2
desorption	5.860	1.101E-3	11.32	14.89	1.386	15.74	5.755	0.927

*The unit is [mol/kg];

†The unit is [1/K];

‡The unit is [K].

Table 2 Parameters of the CO₂ adsorption isotherm model on alumina F200

q_s [mol/kg]	k_{m2} [1/K]	p_{s2} [atm]	Relative Error [%]
9.854	1.319e-3	exp[(T-303)/42.17+5.960]	1.77

Table 3 Boundary conditions for feed, blowdown and purge step

Step	Boundary at the bottom end		Boundary at the top end	
feed	$y_i = y_{feed,i}$	$T = T_{feed}$	$\partial y_i / \partial x = 0$	$\partial T / \partial x = 0$
blowdown	$\partial y_i / \partial x = 0$	$\partial T / \partial x = 0$	$\partial y_i / \partial x = 0$	$\partial T / \partial x = 0$
purge	$\partial y_i / \partial x = 0$	$\partial T / \partial x = 0$	$y_i = y_{purge,i}$	$T = T_{purge}$

Table 4 Properties used in the mathematic model

Property	Value
Bed height, L [m]	2.0
Bed diameter, d_b [m]	0.2
Pellet diameter, d_p [mm]	1.8
Pellet tortuosity, τ	1.5[*]
Pellet porosity, ε_p	0.60[*]
Mean radius of pores, r_{pore} [Å]	45[*]
Bulk porosity, ε	0.37
Bulk density, ρ_b [kg/m^3]	870
Molecular diffusivity, D_m [mm^2/s]	2.375[※]
H$_2$O Adsorption heat, ΔH_{H2O} [kJ/mol]	54.0[†]
CO$_2$ adsorption heat, ΔH_{CO2} [kJ/mol]	33.5[†]
Gas specific heat, $c_{p,g}$ [J·kg^{-1}·K^{-1}]	1005
Solid specific heat, $c_{p,s}$ [J·kg^{-1}·K^{-1}]	784
Axial conductivity, λ_{ax} [W·m^{-1}·K^{-1}]	0.75[‡]

[*]: obtained from Desai et al. 1992.

[※]: obtained from Bird et al. 2002.

[†]: obtained from Rege et al. 2001.

[‡]: obtained from Yagi et al. 1964.

Table 5 Operating Conditions

Operating Condition	Value
Feed air flow rate [Nm^3/h]	120
Feed air temperature [℃]	30
Feed air pressure [bar]	6[a], 10[b]
CO_2 concentration in feed air [ppm]	370
H_2O relative humility in feed air [%]	100
H_2O concentration in feed air [ppm]	6972[a],4180[b]
Purge gas pressure [bar]	1.1
Purge gas temperature [℃]	30, 60, 120, 200

a: case a

b: case b

Table 6 Duration of each step

Case	Feed pressure [bar]	Feed flow rate [Nm³/h]	Feed [min]	Blowdown [min]	Purge [min]
a	6	120	59.0	2	57.0
b	10	120	96.4	2	94.4

Table 7 Desorption performance analysis for case a

Purge gas temperature [℃]	30		60		120		200	
	H_2O	CO_2	H_2O	CO_2	H_2O	CO_2	H_2O	CO_2
Total uptake at the end of feed step [mol]	36.71	1.947	36.71	1.947	36.71	1.947	36.71	1.947
Heat produced by adsorption [kJ]	1982	65.24	1982	65.24	1982	65.24	1982	65.24
Uptake changes in the cycle [mol]	27.00	1.252	31.15	1.645	36.48	1.947	36.71	1.947
Heat consumed by desorption [kJ]	1458	41.94	1682	55.12	1970	65.23	1982	65.24
Introduced heat [kJ]	0		2003		6046		11570	
Desorbed/adsorbed amount ratio [%]	73.55	64.27	84.86	84.49	99.36	99.99	100	100

Table 8 Desorption performance analysis for case b

Purge gas temperature [℃]	30		60		120		200	
	H_2O	CO_2	H_2O	CO_2	H_2O	CO_2	H_2O	CO_2
Total uptake at the end of feed step [mol]	35.82	3.168	35.82	3.168	35.82	3.168	35.82	3.168
Heat produced by adsorption [kJ]	1934	106.1	1934	106.1	1934	106.1	1934	106.1
Uptake changes in the cycle [mol]	30.97	2.353	34.53	2.996	35.82	3.168	35.82	3.168
Heat consumed by desorption [kJ]	1673	78.83	1865	100.4	1934	106.1	1934	106.1
Introduced heat [kJ]	0		3318		10010		19150	
Desorbed/adsorbed amount ratio [%]	86.47	74.27	96.40	94.56	100	100	100	100

Fig. 1 Pressure change with time in the studied cycle (0~t_1 is feed step, t_1~t_2 is blowdown step, t_2~t_3 is

purge step).

Fig. 2 Fitting of the H$_2$O adsorption/desorption equilibrium data on alumina F200 (the multiple lines are

results of fitting at temperature of 5, 15, 25, 35 ℃).

Fig. 3 Fitting of CO_2 adsorption isotherm data on alumina F200.

Fig. 4 Different branches of the H_2O desorption isotherm at 30 ℃.

Fig. 5 Distribution of concentration along the bed height for H_2O and CO_2 at the end of feed step in both

cases investigated in present study.

Fig. 6 Variation of total uptake with time for H_2O and CO_2 during one cycle in both cases investigated in

present study.

Fig. 7 Distribution of temperature and uptakes of H_2O and CO_2 along the bed height at the ends of feed step

and purge step in both cases investigated in present study.

Fig. 8 Variation of dimensionless total adsorbed amount in the bed with dimensionless desorption time for H_2O and CO_2 in both cases investigated in present study.

Fig. 9 Dimensionless adsorption/desorption isotherm for H_2O and CO_2 at 30 ℃

Fig. 10 Distribution of temperature and uptakes of H_2O and CO_2 along the bed height at 1/6, 1/3, 2/3 and 1/1 of desorption time in case a (solid lines, 30 ℃; dashed lines, 60 ℃; dotted lines, 120 ℃; dash-dotted lines, 200 ℃).

Fig. 11 Variation of dimensionless total adsorbed amount in the bed for H_2O and CO_2 with dimensionless

desorption time under different purge gas temperature in case a.

Fig. 12 Energy balance analysis on an elementary volume of the bed during purge step (**Fig. a**: normal temperature profile along the bed height; **Fig. b**: idealized temperature profile along the bed height neglecting heat transfer resistance and axial thermal dispersion).
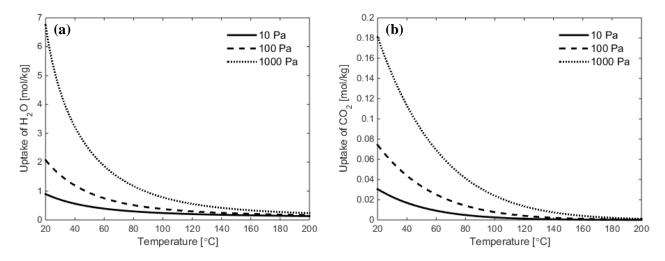
Fig. 13 Variation of equilibrium uptake with temperature for H_2O and CO_2 under different partial pressure.
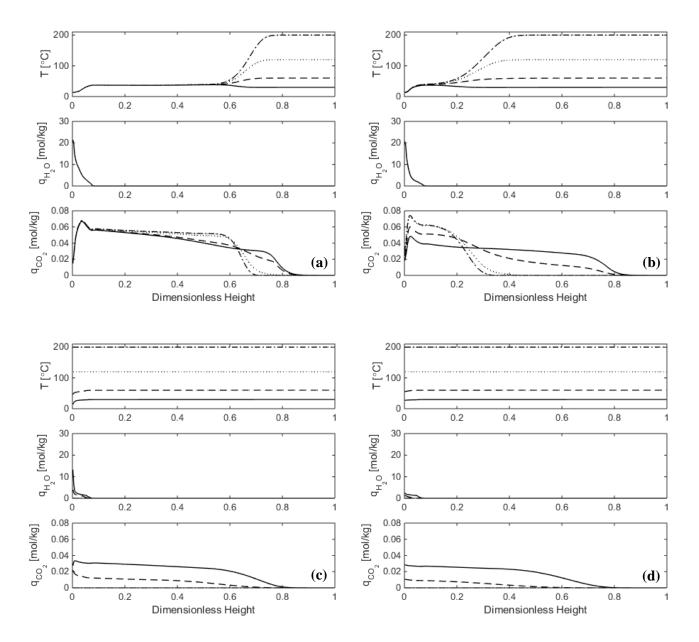
Fig. 14 Distribution of temperature and uptakes of H_2O and CO_2 along the bed height at 1/6, 1/3, 2/3 and 1/1 of desorption time in case b (solid lines, 30 ℃; dashed lines, 60 ℃; dotted lines, 120 ℃; dash-dotted lines, 200 ℃).
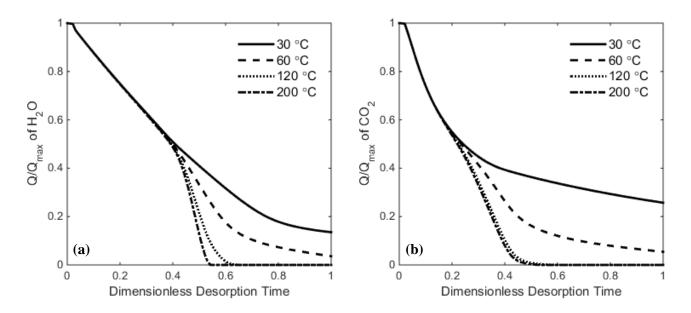
Fig. 15 Variation of dimensionless total adsorbed amount in the bed for H_2O and CO_2 with dimensionless

desorption time under different purge gas temperature in case b.